

## The Response of the Subtropical Front to Changes in the Southern Hemisphere Westerly Winds—Evidence From Models and Observations

 Erik Behrens<sup>1</sup>  and Helen Bostock<sup>2</sup> 
<sup>1</sup>National Institute of Water and Atmospheric Research, Wellington, New Zealand, <sup>2</sup>The University of Queensland, Brisbane, QLD, Australia

### Key Points:

- Stronger westerly winds shift the Subtropical Front (STF), due to enhanced Ekman transports, northward, except in regions of strong currents
- The shift of the STF (2004–2019) is smaller than the shift in the westerly winds, possibly due to increased Ekman transports
- Southward shifts of the STF triggers a positive chlorophyll-a response south of the front, and a negative response north of the front

### Supporting Information:

Supporting Information may be found in the online version of this article.

### Correspondence to:

 E. Behrens,  
[erik.behrens@niwa.co.nz](mailto:erik.behrens@niwa.co.nz)

### Citation:

 Behrens, E., & Bostock, H. (2023). The response of the Subtropical Front to changes in the Southern Hemisphere westerly winds—Evidence from models and observations. *Journal of Geophysical Research: Oceans*, 128, e2022JC019139. <https://doi.org/10.1029/2022JC019139>

Received 27 JUL 2022

Accepted 25 JAN 2023

### Author Contributions:

**Conceptualization:** Erik Behrens, Helen Bostock

**Methodology:** Erik Behrens, Helen Bostock

**Writing – original draft:** Erik Behrens, Helen Bostock

**Writing – review & editing:** Erik Behrens, Helen Bostock

**Abstract** The location of the Subtropical Front (STF), the boundary between Subtropical and Subantarctic Water in the Southern Ocean is proposed to be influenced by the strength and location of the Southern Hemisphere westerly winds. We use a hydrodynamic hindcast model and recent observations to test if changes in the westerly winds can cause meridional shifts in the STF over interannual to decadal timescales by modulating local Ekman transport. We find that increased, or northward, shifted westerly winds lead to an enhanced northward Ekman transport over large parts of the Southern Ocean, resulting in a northward shift in the STF. Conversely for weaker or southward shifted westerly winds where the STF migrates south. However, this relationship breaks down in regions with strong eddy variability and western boundary current systems. In these regions an increase in westerly winds lead to a southward shift in the STF. Observation data from 2004 to 2019 display a southward shift of STF associated with the positive Southern Annular Mode. However, the shift is smaller than the latitudinal shifts in the location of the zero wind stress curl and maximum westerly winds ( $-0.4^\circ$  latitude/decade). This discrepancy is due to positive Ekman trends resulting from the intensification of the westerly winds, which oppose the southward migration. Changes in the Ekman transport and the overall southward shift of the STF have also resulted in an observed positive trend in chlorophyll-a concentrations south of the STF, which could have ramifications for marine ecosystems and the biological pump in the Southern Ocean.

**Plain Language Summary** The Subtropical Front (STF) is an important water mass barrier, between warm, salty, and nutrient-depleted Subtropical Waters of the subtropical gyre to its north, and cold, fresh, but nutrient-rich Subantarctic Waters of the Southern Ocean to its south. The position of the STF is thought to be influenced by the westerly winds. In this study we investigate if the STF shifts in relation to changes in these westerly winds. Our model experiments show that over large parts of the Southern Ocean, the changes in the location of the STF follow changes in the westerly winds, except in regions of strong oceanic currents. The observations show that between 2004 and 2019 a small southward trend of the STF has been detected over most parts of the Southern Ocean as a consequence of southward shift of the westerly winds due to positive Southern Annular Mode (SAM). However, the shift in the STF has not been as large as the shift in the winds, as it has been opposed by the strengthening of the westerly winds. The recent southward shift in the STF has led to an increase in plankton growth south of the STF due to increased mixing of the Subtropical and Subantarctic Waters.

## 1. Introduction

The Subtropical Front (STF) marks the water mass boundary between warm, salty and nutrient-depleted Subtropical Water in the subtropical gyre to its north, and cold, fresh, and nutrient-rich Subantarctic Waters in the Southern Ocean to its south (Belkin, 2021; Belkin & Gordon, 1996; Chapman et al., 2020; Deacon, 1982; Orsi et al., 1995; Sokolov & Rintoul, 2009). As such the STF is often used as the northern boundary of the Southern Ocean. Due to the mixing of these two water masses the STF is a hotspot for primary production seen by elevated levels of chlorophyll-a (Chiswell et al., 2013; Pinkerton et al., 2005; Sullivan et al., 1993; Weeks & Shillington, 1994), and therefore also important for carbon sequestration and fisheries.

The location of the STF is proposed to be influenced by the strength and location of the Southern Hemisphere westerly winds. However, the exact position of the STF is still not fully understood, since its location does not align with the theory that it should co-locate with the line of zero wind stress curl (De Boer et al., 2013; Tilburg

© 2023. The Authors.

 This is an open access article under the terms of the [Creative Commons Attribution License](https://creativecommons.org/licenses/by/4.0/), which permits use, distribution and reproduction in any medium, provided the original work is properly cited.

et al., 2002). This knowledge gap motivated a range of research and has led to an alternative definition of the Subtropical Front, the so called Dynamical Subtropical front, which links the STF to ocean dynamics rather than to water mass properties (De Boer et al., 2013; Graham et al., 2012). Furthermore, recent research suggests that the STF will show a poleward shift as a consequence of expanding subtropical gyres due to positive Southern Annual Mode (SAM) trends shifting the southern hemisphere westerly winds south over multi-decadal timescales (Yang et al., 2020). However, equatorward shifts of the STF have also been reported, challenging the potential drivers of shorter, sub-decadal shifts (Yang et al., 2020). Recent results by Caneill et al. (2022) also suggest that changes in the buoyancy forcing can alter the location of the boundary between subtropical and subantarctic gyre.

In this paper we investigate the drivers of STF variability on interannual to decadal timescales using a combination of Argo, satellite, and hindcast datasets. Here we define the STF by the 11°-isotherm at 100 m depth following Orsi et al. (1995). In particular we test if changes in STF location can be attributed to local changes in the Ekman transport, as a consequence of changes in the westerly winds (meridional shift, or changes in the strength of the winds, Figure 1).

Based on Ekman theory (Knauss & Garfield, 2016) an increase in surface (zonal) winds would result in a stronger local Ekman transport (Figure 1b), which carries more cold Subantarctic Waters northward and would trigger a northward shift of the STF (Rintoul & England, 2002). The negative sea surface temperature (SST) anomalies would cause a positive heat flux anomaly (into the ocean) trying to compensate for the advection of cold water northward. Associated changes in the wind stress curl increase the Ekman pumping north of the STF and results in steeper isotherms, but may not necessarily generate a shift in the STF at 100 m depth. Furthermore, these negative SST anomalies would lead to negative chlorophyll-a (Chl-a) anomalies in Subantarctic Waters and an increase in Subtropical Waters, relative to the time-mean location of the STF. In Subtropical waters a further warming increases the stratification which reduces the nutrient supply and triggers a decline in Chl-a. In the Subantarctic Waters deep mixed layers and/or mixing causes light to be the limiting factor for phytoplankton growth. An increase in stratification and shallower mixed layers, due to warming, therefore leads to positive Chl-a anomalies (Boyd, 2002; Bradford-Grieve et al., 1999). This concept follows previous work in the Southern Ocean (Lovenduski & Gruber, 2005), but has been applied to the STF in this paper.

In the case of southward shifting winds (Figure 1c) local Ekman transport declines, which initiates a southward shift of the STF. Consequently, that leads to negative heat flux anomalies (out of the ocean) and an increase in Chl-a concentration to the south of the STF and a decline to its north. However, a reduction in Ekman pumping north of the STF shoals the isotherms, but, again it may not impact the location of the STF at 100 m water depth.

In this paper we use hydrodynamic hindcast and idealized simulations with individual changes to the wind forcing using the NZ20 model (Behrens et al., 2021) in combination with in-situ and remotely sensed observation data from 2004 to 2019 to test these conceptual models (Figure 1).

The paper is organized as follows: Section 2 introduces the data sources and methods. Section 3.1 summarizes the results from sensitivity simulations where surface winds have been deliberately altered. Section 3.2 highlights where Ekman transports can be used to explain interannual variability of the STF in the Southern Ocean between 2004 and 2019 and Section 3.3 provide insights into long-term trends. Section 4 provides a conclusion and discussion.

## 2. Methods

### 2.1. Model Simulation

This study uses data from a global eddy permitting configuration, with a nominal resolution of ¼ degree, which is known as GO6, and details of this configuration for this global setup can be found in Storkey et al. (2018). Ocean physics are simulated by NEMO 3.6 (Madec et al., 2017), while CICE version 5.2.1 (Hunke & Lipscomb, 2010) has been used for sea-ice. Vertical mixing in this configuration is simulated through a turbulent kinetic energy scheme (Gaspar et al., 1990; Madec et al., 2017). In the southwest Pacific this model produces a cold and fresh bias over the Tasman Sea, which has led to northward displacement of the STF in the model compared to the observations (Behrens et al., 2021). By embedding a high-resolution (1/20°, NZ20) nested grid into the GO6 configuration this model bias was reduced and the STF better simulated (Behrens et al., 2021). The nested region spans only the ocean around New Zealand from 142.8°E to 152°W and 59° to 22°S with a grid spacing of about

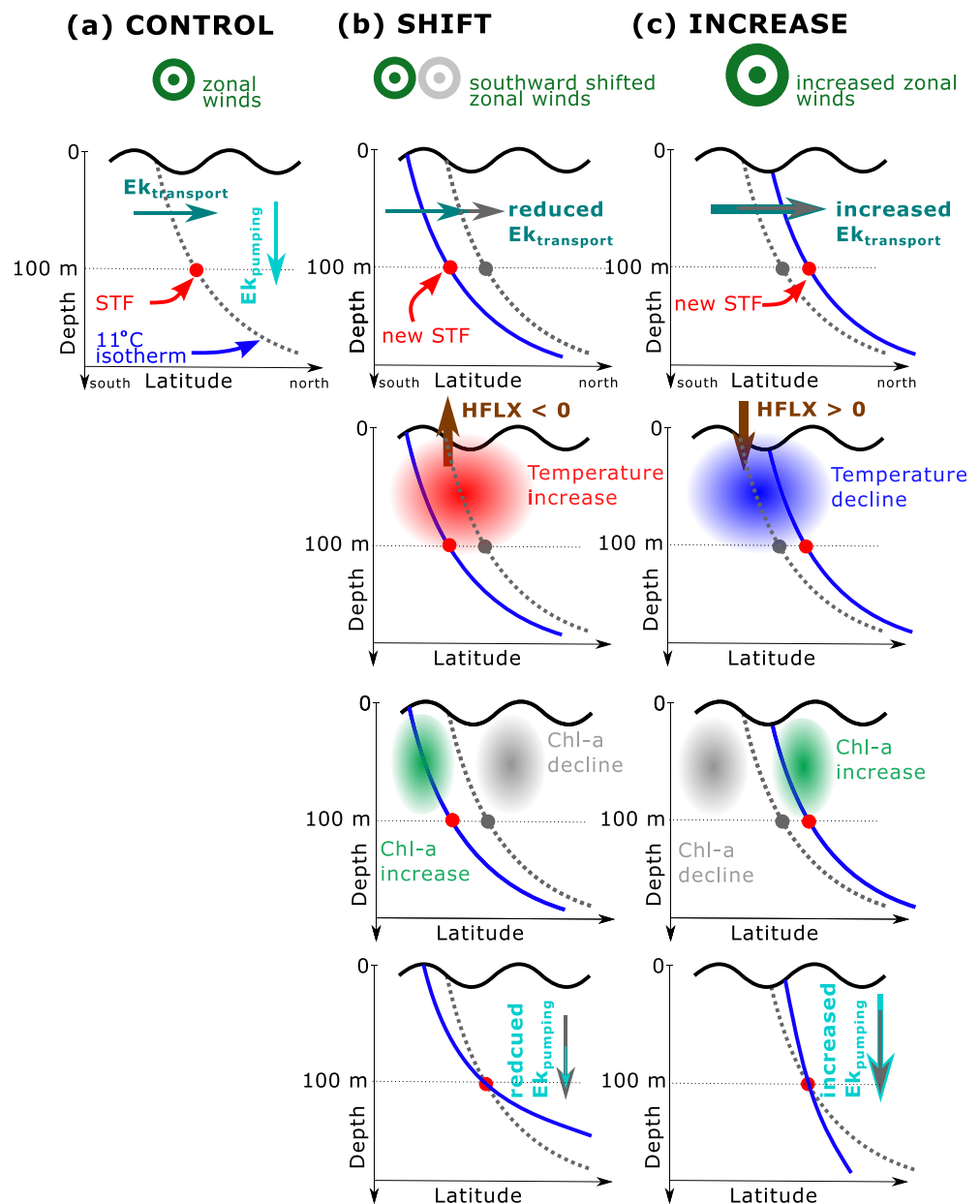


**Figure 1.** This Schematic shows how changes in surface winds are expected to alter the location of the STF following the Ekman theory. Panel (a) for the CONTROL, (b) for a southward shift of the westerly winds and (c) for an increase in westerly winds in relation to CONTROL. The gray dashed lines mark the 11°-isotherm in CONTROL and the red dots showing the location of the STF at 100 m depth (as defined by Orsi et al. (1995)) in the individual simulations. In (b) and (c) the gray dotted lines, gray dots, and gray circles are the 11° isotherm, STF location and winds from the CONTROL case. In (b) a southward shift of the winds leads to negative Ekman transport anomalies, and a southward shift of the STF is accompanied by positive temperature anomalies. These temperature anomalies trigger positive heat flux anomalies (HFLX, from the ocean to the atmosphere) and cause a decline of Chl-a north of the STF<sub>CONTROL</sub> and an increase to its south. However, reduced Ekman pumping shoals the isotherms, but may not impact the location of the STF. (c) An increase in the strength of the westerly winds leads to positive Ekman transport anomalies, and a southward shift of the STF accompanied by negative temperature anomalies and negative heat flux anomalies (from the atmosphere into the ocean). The negative SST anomalies result in negative Chl-a anomalies south of the STF<sub>CONTROL</sub> and positive anomalies to the north. An increase in Ekman pumping results in a steepening of the isotherms, but may not shift the STF.

4 km to fully resolve mesoscale processes. NZ20 demonstrated a better performance for past variability in the STF around New Zealand (Behrens et al., 2021). Even though the nested region only covers a small portion of the circumpolar study area, the better performance of NZ20 over the stand alone GO6 configurations motivated

the use for this study. Computational and human resources prevented us from expanding the nested domain to the entire circumpolar study area. The nesting of NZ20 has been facilitated by a two-way nesting scheme based on AGRIF (Debreu et al., 2008). The vertical dimension is discretized by 75-vertical  $z$ -levels, with a 1 m thick surface layer which increases to about 200 m in the deep ocean. The model uses a non-linear free surface and a partial cell approach to improve bottom flows (Barnier et al., 2006). This global nested NZ20 configuration simulates boundary current transports (Table S1 in Supporting Information S1) and the STF in good agreement to observations (Belkin, 2021).

In this nested NZ20 setup a 62-year long model hindcast, from 1958 to 2019 has been conducted, using JRA55-DO v1.5 (Tsujino et al., 2018) atmospheric boundary conditions, hereafter CONTROL. This product provides surface winds (zonal and meridional), air temperature, humidity, short and long wave radiation, snow, and precipitation as 3-hourly averages at the ocean surface. Bulk formula (Griffies et al., 2009) are used to generate surface fluxes, which are then applied to force the ocean.

The simulation has been started from rest with temperature and salinity fields based on the EN4 climatology (Good et al., 2013). A coastal runoff climatology has been applied, and sea surface salinity has been restored to the EN4 climatology with timescales of 30 days for the 1 m thick surface layer. In addition to the CONTROL, two sensitivity simulations have been conducted where changes to the surface southern hemisphere westerly winds, have been applied. These simulations cover the period from 2000 to 2019 to test how changes in the surface winds impact the location of the STF. It is assumed that a period of 20 years is sufficient to detect a robust response in these sensitivity simulations in comparison to CONTROL.

In the first simulation a southward shift of the southern hemisphere westerly winds of 1-degree latitude per decade has been applied uniformly to zonal and meridional winds, hereafter **SHIFT** (Figure S1 in Supporting Information S1). This has been done by shifting winds between 70° and 25°S incrementally southward. To minimize potential discontinuities at the northern and southern boundary a linear interpolation over 5° latitude has been applied over the boundary. Adjusting zonal and meridional winds in the same way reduces the distortion of storms, which can otherwise result in artificial wind-stress curl anomalies (Frankcombe et al., 2013). In the second simulation a positive increase in wind strength of 1% per year has been applied uniformly to zonal and meridional winds, hereafter **INCREASE** (Figure S1 in Supporting Information S1). This has been done by incrementally increasing winds between 70° and 25°S according to their local wind speeds. While the relative change is uniform across the latitude band, the absolute change of the wind speeds is spatially varying, where larger winds in CONTROL lead to a larger absolute increase in INCREASE. A linear interpolation, identical to SHIFT, has been applied at the northern and southern boundary over 5° latitude.

Applying incremental shifts and increases instead of step changes to winds, as done in previous studies (Frankcombe et al., 2013; Spence et al., 2010, 2014), was motivated to avoid initial shocks and to reduce the likelihood of spurious deep convection in the Southern Ocean (Behrens et al., 2016), which could also influence the STF response to these wind perturbations. The JRA55-DO v1.5 winds show over the period 2000–2019 in CONTROL an increase in zonal winds between 0% and 0.6% per year, which varies by latitude (Figure S2 in Supporting Information S1). Over this period the location of the maximum of the zonal winds also shows a southward trend of 0.4° latitude per decade. These JRA55-DO values are in-line with previous estimates (see Swart & Fyfe, 2012). The imposed trends in the experiments SHIFT and INCREASE are larger than the observed trends between 2000 and 2019 and intended to understand the general response to shifted or increased winds. However, there are some possible issues with forced models as the unavoidable thermal restoring (due to unchanged air temperatures) might limit the STF response to artificial wind changes (see discussion).

## 2.2. Additional Data Sources and Metrics

The Roemmich-Gilson Argo climatology (Roemmich & Gilson, 2009), hereafter referred to as Argo, has been used for the comparison to model temperatures and model STF location. Furthermore, Chl-a from MODIS satellite (Sathyendranath et al., 2019) mission has been used to link Chl-a anomalies to meridional shifts in the location of the STF. The monthly mean MODIS satellite data was linearly interpolated onto a regular 1° × 1° grid to allow for a direct comparison to the Argo results, which are also provided on a regular 1° × 1° grid.

We apply the Orsi et al. (1995) water mass definition to locate the STF, which uses the 11°C isotherm at 100 m depth. By using temperatures at 100 m depth to define the STF instead of using SSTs the seasonal variability is

reduced (Orsi et al., 1995). Furthermore, temperature anomalies averaged over the top 100 m have been calculated to link them to Ekman transports and to meridional shifts of the STF. Using the averaged top 100 m temperature was motivated by Ekman depths of about 75–100 m at this latitude (Lenn & Chereskin, 2009; Wang & Huang, 2004), and the STF defined as the 11°C isotherm at 100 m (Orsi et al., 1995). This choice also reduces the impact of the SST “restoring” of ocean-only models. All data sources (model and observational data) are available as monthly means, but were annually averaged to investigate interannual variability between years.

For the two wind perturbation sensitivity simulations, we have evaluated meridional shifts of the STF, Ekman transports, surface heat fluxes and Ekman pumping over the entire Southern Ocean. We focus on the data over the last 5 years of the simulation (2015–2019) relative to the CONTROL simulation to detect forcing related changes over intrinsic variability.

To test the STF response, following Figure 1, anomalies for the averaged top 100 m temperatures, surface heat fluxes, Ekman transports, Ekman pumping, mixed layer depths (MLD), potential vorticity and meridional 100 m temperature gradient have been computed over a latitudinal range of  $\pm 2.5^\circ$  latitude over the time mean STF location for each longitude (2004–2019, hereafter STF<sub>CONTROL</sub>, black line in Figure 2a). This has been performed for model data for every zonal grid box on the global model grid (1,440 locations,  $\sim 20$  km spacing), before averaging the meridional means zonally over  $5^\circ$  longitude bands. For Argo and Chl-a the procedure was repeated, but using a  $1^\circ$  grid (zonal 360 grid boxes). MLDs have been identified as depths where the potential density difference exceeds  $0.01 \text{ kg/m}^3$  compared to the surface layer. Potential vorticity has been calculated using the local Coriolis parameter divided by the local water depth. Chl-a anomalies have been computed for a  $5^\circ$  latitude band south of the mean STF location (see Figures S3 and S4 in Supporting Information S1).

### 3. Results and Discussion

#### 3.1. Wind Sensitivity Simulations

Both SHIFT and INCREASE simulations show changes in the location of the STF of  $\pm 2^\circ$  in latitude over the last 5 years of the simulation (2015–2019) in comparison to CONTROL (Figures 2a and 2b). In INCREASE (blue lines/dots) the displacement of the STF is predominantly northward, in agreement with Figure 1. In SHIFT, the STF migrates predominantly southward, but considerably less than expected compared to the applied  $2^\circ$  degree shifted winds by the end of 2019. In both sensitivity simulations the STF response is not-uniform with longitude (Figure 2b). Furthermore, the magnitude of meridional displacement in either INCREASE or SHIFT simulations is not linked to changes in ocean bathymetry (gray shading, represented by potential vorticity). This differentiates the surface intensified STF from other fronts in the Southern Ocean, which are directly influenced by bottom topography due to their barotropic nature (Thompson & Sallée, 2012). The regions where the sign of the STF anomaly aligns with the sign of the Ekman anomaly (Figure 1) are represented by filled circles in Figure 2b. In SHIFT the STF response follows the proposed Ekman transport (red filled circles in Figure 2b) over parts of the Agulhas region, the central Indian Ocean, south of Australia to  $160^\circ\text{E}$ , over small parts of the central Pacific Ocean ( $\sim 130^\circ\text{W}$ ), the eastern Pacific Ocean and east of the Malvinas Current. In INCREASE, similar regions to SHIFT show an agreement between the STF response and the Ekman transport (blue filled circles), but not for the regions influenced by western boundary currents. The different behavior for the boundary currents can be explained by the Sverdrup balance, with an increase in basin-wide wind stress curl in INCREASE (Figure S5c in Supporting Information S1 shows Ekman pumping which is based on wind stress curl). That leads to an increase in the strength of the western boundary currents, which shifts the STF southward in these regions, against the local enhanced northward Ekman forcing (Figure S6c in Supporting Information S1). In SHIFT the impact on western boundary currents and open ocean currents is the same and both tend to shift south.

The surface heat flux anomalies (Figure 2c and see Figure S7 in Supporting Information S1) over the STF<sub>CONTROL</sub> co-vary in most regions with the sign and magnitude of the STF displacement from Figure 2b in SHIFT (red filled circles). In INCREASE, exceptions (blue circles) occur in regions of high mesoscale activity, illustrated by sea surface height variance (gray shading in Figure 2c). Regions of high mesoscale activity are between  $60^\circ$  and  $70^\circ\text{E}$ , part of the Agulhas Return Current, around  $100^\circ\text{E}$  where a branch of the Super Gyre crosses the STF, around  $150^\circ\text{E}$  where the East Australian Current Extension overshoots, around  $180^\circ$  where the STF detaches from the Chatham Rise, around  $110^\circ\text{W}$  in middle of the Pacific Ocean and at  $30^\circ\text{W}$  within the Malvinas Current. These regions of alignment with Figure 1 overlap with regions identified in Figure 2b.

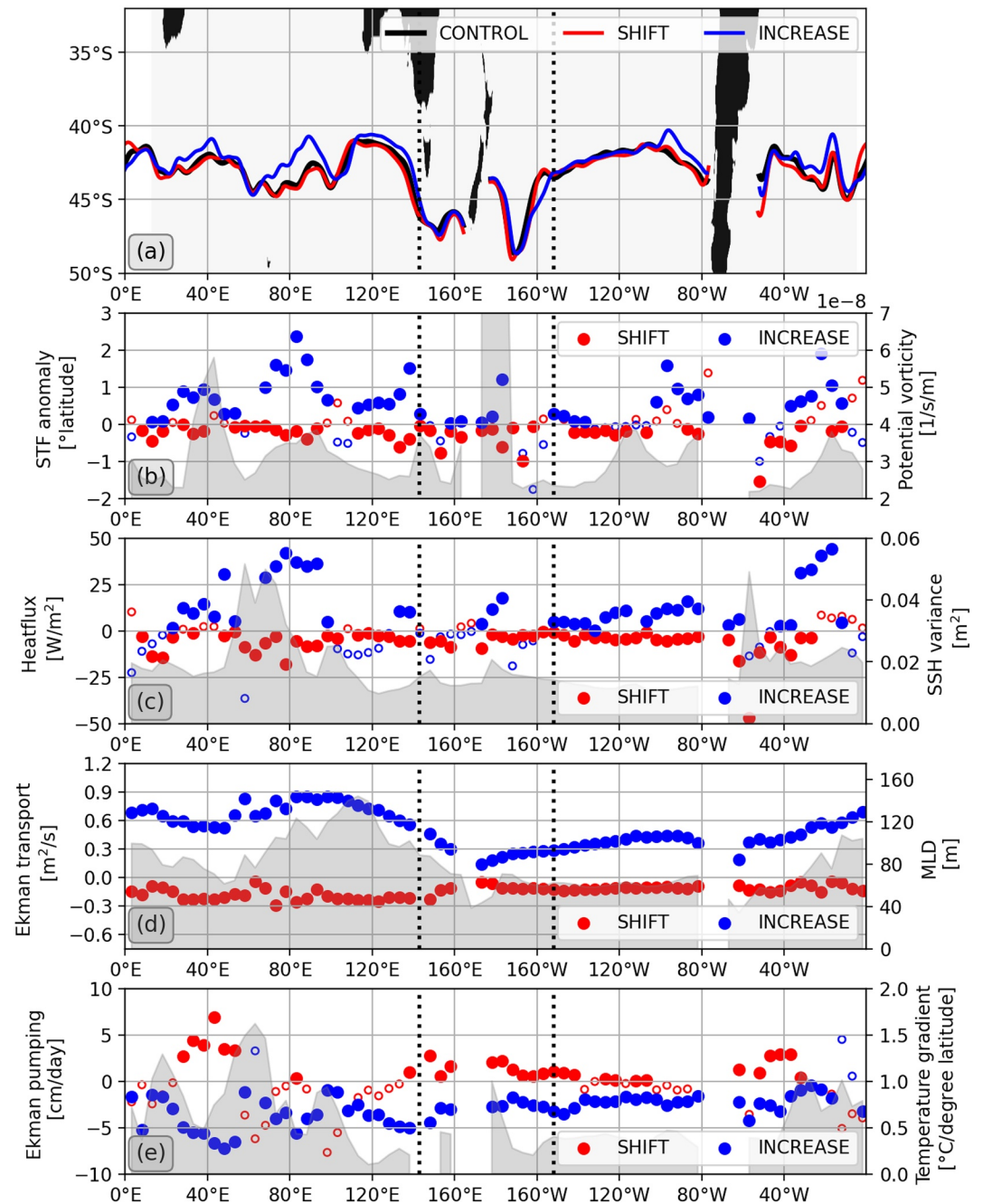


**Figure 2.** 2015–2019 anomalies for INCREASE and SHIFT (southward) relative to CONTROL: (a) STF location, (b) STF location anomaly and potential vorticity ( $f/h$ , gray shading) from CONTROL, (c) surface heat flux anomaly and mean sea surface height (SSH) variance (gray shading) from CONTROL, (d) Ekman transport anomaly and mean mixed layer depth (MLD, gray shading) from CONTROL, (e) Ekman pumping anomaly and meridional 100 m temperature gradient (gray shading) from CONTROL. The anomalies are computed over the time mean path ( $\pm 2.5^\circ$  latitude) of the STF<sub>CONTROL</sub>. Filled circles indicate where the sign of anomalies aligns with Figure 1 schematic, open circles indicate the opposite behavior. Results in (b–e) have been zonally averaged over  $5^\circ$  longitude bins. The two dashed vertical black lines show the eastern and western boundary of nested region in NZ20, where model resolution has been refined around New Zealand.

The sign of the induced Ekman transport anomalies aligns with Figure 1 (filled circles in Figure 2d and see Figure S6 in Supporting Information S1), while the magnitude varies zonally due to the actual strength of the zonal winds and the pathway of the STF. The magnitude of the Ekman transport anomalies does not correlate with the magnitude of meridional STF shift, locally. Nevertheless, the overall Ekman transport anomaly in INCREASE

is larger in comparison to SHIFT and consequently a larger STF displacement is seen in INCREASE compared to SHIFT. Furthermore, the largest Ekman transport anomalies are located over the Indian Ocean in INCREASE and SHIFT, which is also the ocean basin showing the largest meridional STF shift. In addition, this is also the region with the deepest MLDs for the STF of about 130 m (gray shading). MLDs of about 100 m or deeper would allow that surface heat flux anomalies and heat advection to directly influence the location of the STF, while shallower MLDs would prevent this direct impact. MLDs over the central Pacific and eastern Pacific Ocean are only 60 m deep, which may explain the smaller STF changes in the Pacific Ocean. This would suggest that surface heat fluxes and heat advection alone cannot penetrate deep enough to impact the STF directly, and potentially limit the STF response in these regions.

The Ekman pumping response aligns with Figure 1 for INCREASE for most longitudes, but less so for SHIFT (Figure 2e, see also Figures S5 and S8 in Supporting Information S1). Reasons for the discrepancy in SHIFT might be due to an overall smaller applied perturbation in SHIFT, compared to INCREASE, which might not be large enough to overcome the intrinsic variability. The meridional temperature gradient (gray shading) is elevated in regions with higher mesoscale variability and restricts the meridional shift of the STF. A smaller meridional temperature gradient would allow for a larger meridional displacement of the STF with the same perturbation applied.

Overall, these sensitivity tests suggest a link between STF displacement and local Ekman transport in regions away from energetic western boundary currents. While the direction of displacement follows the sign of the Ekman transport anomalies, the local magnitude of STF displacement cannot be directly attributed to the magnitude of Ekman transport anomaly. Here, the local oceanographic conditions, such as horizontal temperature gradient and presence of oceanic currents also impact the magnitude of the displacement. The applied wind anomalies are stronger than the observed natural trends and therefore the initiated response might be stronger than in the real world. Nevertheless, the actual modeled STF response to these wind anomalies was weaker than expected due to the dampening effect of the thermal restoring, by prescribing the same SSTs across all simulations. We have defined the STF by the 11°C isotherm at 100 m depths (Orsi et al., 1995), which reduces the impact of the thermal restoring. However future studies could use fully coupled models to evaluate the STF response to these wind changes to eliminate this shortcoming.

### 3.2. Drivers of Interannual Observed Variability of the STF

In this section we test if and where this above-described physical conceptual model can be applied to understand the observed interannual variability of the STF between 2004 and 2019 using temperature from Argo floats (Argo data only available from 2004 onwards), and the biological response through satellite observed Chl-a anomalies. In doing so we aim to identify regions where Ekman transport can explain past STF variability, and regions where other drivers are at play.

The observed averaged top 100 m temperature anomalies from Argo show interannual variations in the order of  $\pm 0.8^{\circ}\text{C}$  and an overall positive trend over the period 2004 to 2019 (Figure 3a and see Section 3.3). The modeled averaged top 100 m temperature anomalies align with the observed anomalies (Figure 3b) in time, space and magnitude for most regions (see also Figure S9 in Supporting Information S1). Between 65% and 95% of all times the sign of the anomaly between both data sources agrees with a root-mean square error of about  $0.25^{\circ}\text{C}$ . This good match in the southwest Pacific suggests a good performance of NZ20 to simulate past STF variability (Behrens et al., 2021). The exception is large fluctuations on spatial and interannual scales between  $0$  and  $60^{\circ}\text{E}$ , which is the region impacted by the Agulhas Retroflexion and Return Current, where the root-mean square error is above  $0.3^{\circ}$ .

In particular, the larger modeled temperature anomalies ( $< -0.5^{\circ}\text{C}$ ,  $> 0.5^{\circ}\text{C}$ ) co-align with the sign of the model Ekman transport anomalies (nonwhite squared anomalies in Figures 3b and 3c) as expected from Figure 1. In addition, the magnitude of the Ekman transport anomalies appears to be reflected in the magnitude of the temperature anomalies. The averaged top 100 m temperature anomalies consequently generate a very similar pattern in the meridional displacement of the STF (Figures 4a and 4b) in Argo and in the model. The modeled surface heat fluxes over the STF (Figure 4c) exhibit more variability in space and time than the Ekman transports (Figure 3c). This suggests that the observed heat fluxes are not entirely driven by Ekman transports alone as they are in both sensitivity simulations SHIFT and INCREASE. In the real-world

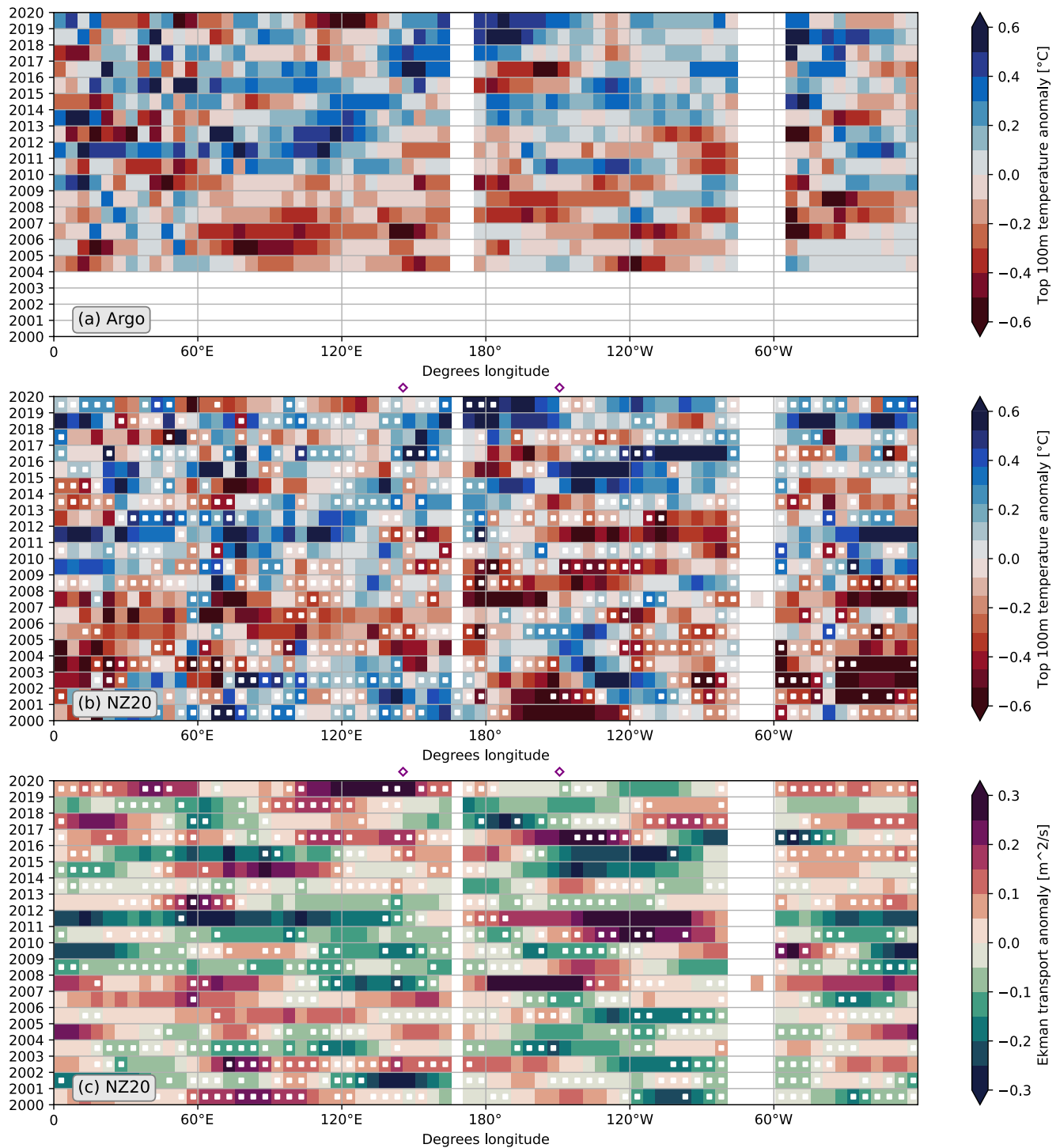


**Figure 3.** (a) Averaged top 100 m Argo temperature anomaly relative to the period 2004–2019. (b) Same as (a) but for NZ20. (c) NZ20 Ekman transport anomaly. White squares in (b) and (c) indicate where the sign of averaged top 100 m temperature and Ekman transport anomalies does not align with the concept in Figure 1. All anomalies (a–c) are extracted over the time mean STF location at each longitude ( $\pm 2.5^\circ$  latitude band, 2004–2019). Observations and model results have been binned to  $5^\circ$  longitude bins. The two purple diamonds in (b) and (c) indicate the eastern and western boundary of nested region in NZ20, where model resolution has been refined around New Zealand.

wind changes also influence surface air temperature anomalies via advection and impact heat flux anomalies. Despite the larger variability, the sign of surface heat flux anomalies and modeled STF displacement aligns with what is expected in Figure 1 in many regions, as shown in Figures 4b and 4c by the nonwhite squared anomalies.

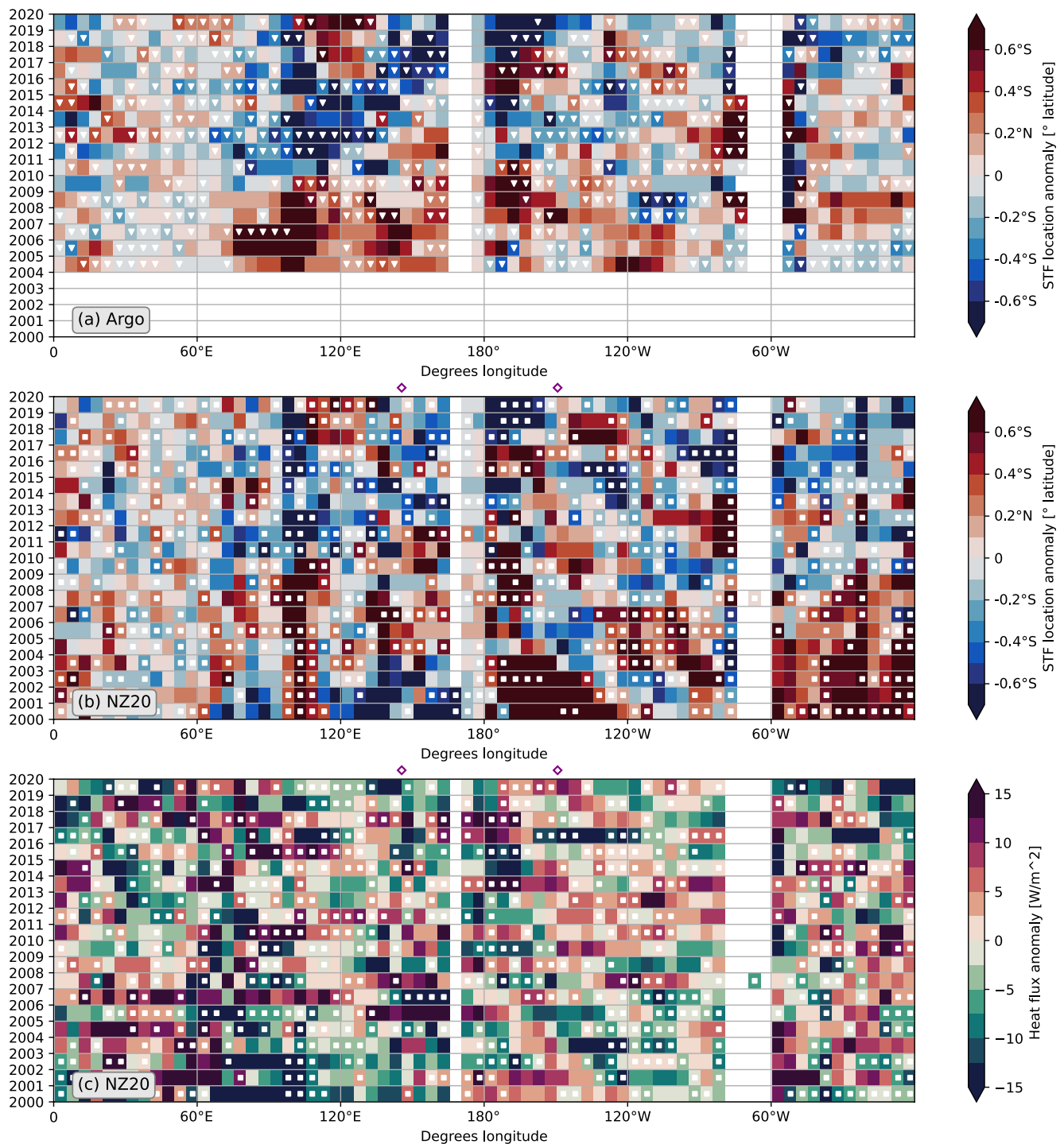


**Figure 4.** (a) Argo meridional STF location anomaly in  $^{\circ}$  latitude relative to the period 2004–2019. (b) Same as (a) but for NZ20. (c) Surface heat flux anomalies from NZ20 where positive anomalies indicate a heat flux into the ocean. White triangles in (a) indicate where the sign of STF location and Chl-a anomalies (Figure 5a) does not align with the concept in Figure 1. White squares in (b) and (c) indicate where the sign of STF location and surface heat fluxes anomalies does not align with the concept in Figure 1. All anomalies (a–c) are extracted over the time mean STF location at each longitude ( $\pm 2.5^{\circ}$  latitude band, 2004–2019). Observations and model results have been binned to  $5^{\circ}$  longitude bins. The two purple diamonds in (b) and (c) indicate the eastern and western boundary of nested region in NZ20, where model resolution has been refined around New Zealand.

We also assessed the biological response in relation to shifts of the STF, by analyzing Chl-a anomalies up to 5° south of the time mean location of the STF (Figure 5a). For most longitudes there is a positive Chl-a trend, which corresponds to the positive temperature trend (Figure 3a and Section 3.3) and an overall southward shift of the STF (Figure 4a) between 2004 and 2019. The sign of Chl-a and STF anomalies on shorter, interannual timescales aligns in many cases with the concept in Figure 1 (nonwhite triangled anomalies in Figures 4a and 5a). This is particularly true for strong ( $<-0.5$  or  $>0.5$  mg/m<sup>3</sup>) Chl-a anomalies.

To assess the overall robustness of the concept in Figure 1 a simple counting of anomalies, which follow the concepts in Figure 1, has been performed over the Southern Ocean for the observed and modeled data between 2004 and 2019 (Figure 5b). The small sample size (16 annual values from 2004 to 2019) restricted more sophisticated methods to be deployed to measure its robustness. Neither parametric nor non-parametric correlation produced significant ( $>95\%$  significant level) relationships for any of the parameters. Nevertheless, the counting suggest that the concepts of Figure 1 apply between 60% and 80% of the time over large parts of the Southern Ocean. Regions where the physical concept follows the concept in Figure 1 (likelihood  $\geq 50\%$  for both physical criteria) are shown by the blue horizontal bar and account for about 70% of the ocean. Regions where the physical concept fails align with regions identified in Figure 2c (gray shading), where mesoscale eddy variability is elevated, for example, at around 60° and 120°E where the STF interacts with the Agulhas Return Current and the southern boundary of the Super Gyre, respectively. The Super Gyre is the combination of the three subtropical gyres in the Southern Hemisphere, diagnosed by the zero line of the barotropic streamfunction, which separates the subtropics from the Antarctic Circumpolar Current.

If we include Chl-a in the assessment criteria together with the physical criteria (orange bars, likelihood  $\geq 50\%$  for all three criteria), the concept still applies to about 55% of the ocean. We acknowledge that the 50% cut-off threshold is an arbitrary choice to prove that the concept applies since an independent normal distributed process should center around 50%. Nevertheless, since these processes are biophysically linked, the probability that they randomly co-occur are unlikely. The geographical coherence of this agreement and disagreement provides further evidence that the concept applies in many regions. However, again his concept fails in regions where the STF interacts with strong western boundary currents and subsequent elevated eddy activity.

### 3.3. Observed Trends in STF Location From Argo SST and Chl-a Between 2004 and 2019

Based on the concept outlined above, a southward shift of the westerly winds would promote a southward shift of the STF, while stronger westerly winds will increase the northward Ekman transport and initiate a northward shift of the STF (see Figure 1 and Section 3.1). The consequence of these factors combined could be that the STF does not shift if both factors balance each other.

The Argo STF trends are mostly small ( $<0.25^\circ$  latitude per decade, black circles in Figure 6a), but show a predominantly southward directed trend following the southward shifted westerly winds. Larger southwards trends ( $>0.5^\circ$  latitude per decade) are seen between 70°–105°E, 130°E–160°W and between 180° and 160°E. The southward shift of the STF goes along with positive Chl-a trends south of the time mean location of the Argo STF at each longitude (green filled circles), as expected with the concept proposed in Figure 1. Nevertheless, the actual Argo STF trends are smaller than the expected STF trend (gray dashed line), based on the changes in the position of the zero wind stress curl (Qu et al., 2019) and the location of the maximum westerly winds (Figure S2d in Supporting Information S1), which both show a southward trend of  $\sim 0.4^\circ$  latitude/decade. We argue that this mis-match, between expected and actual STF trends, is related to changes in local winds (i.e., zonal wind, blue shading) and the consequential Ekman forcing. In regions where the zonal wind trend is positive over the STF, the observed STF trend is smaller than the expected STF trend ( $-0.4^\circ$  latitude/decade) and conversely for negative zonal wind trends. Regions which follow this concept are shown by black filled circles and align with regions of alignment identified in the previous sections. Exceptions (black circles) from the concept again match with regions of elevated eddy variability, or where the STF encounters currents.

The observed southward trend of the STF goes hand in hand with a poleward habitat expansion of subtropical species (Law et al., 2017; Shears & Bowen, 2017) and is related to the observed poleward expansion of the subtropical gyres (Yang et al., 2020). In this context accelerated warming over the western boundary currents has been observed (Li et al., 2022; Wu et al., 2012) and had cascading effects on the marine ecosystems via marine heatwaves (Smale et al., 2019). Our results together with others (e.g., Carranza & Gille, 2015; Del Castillo

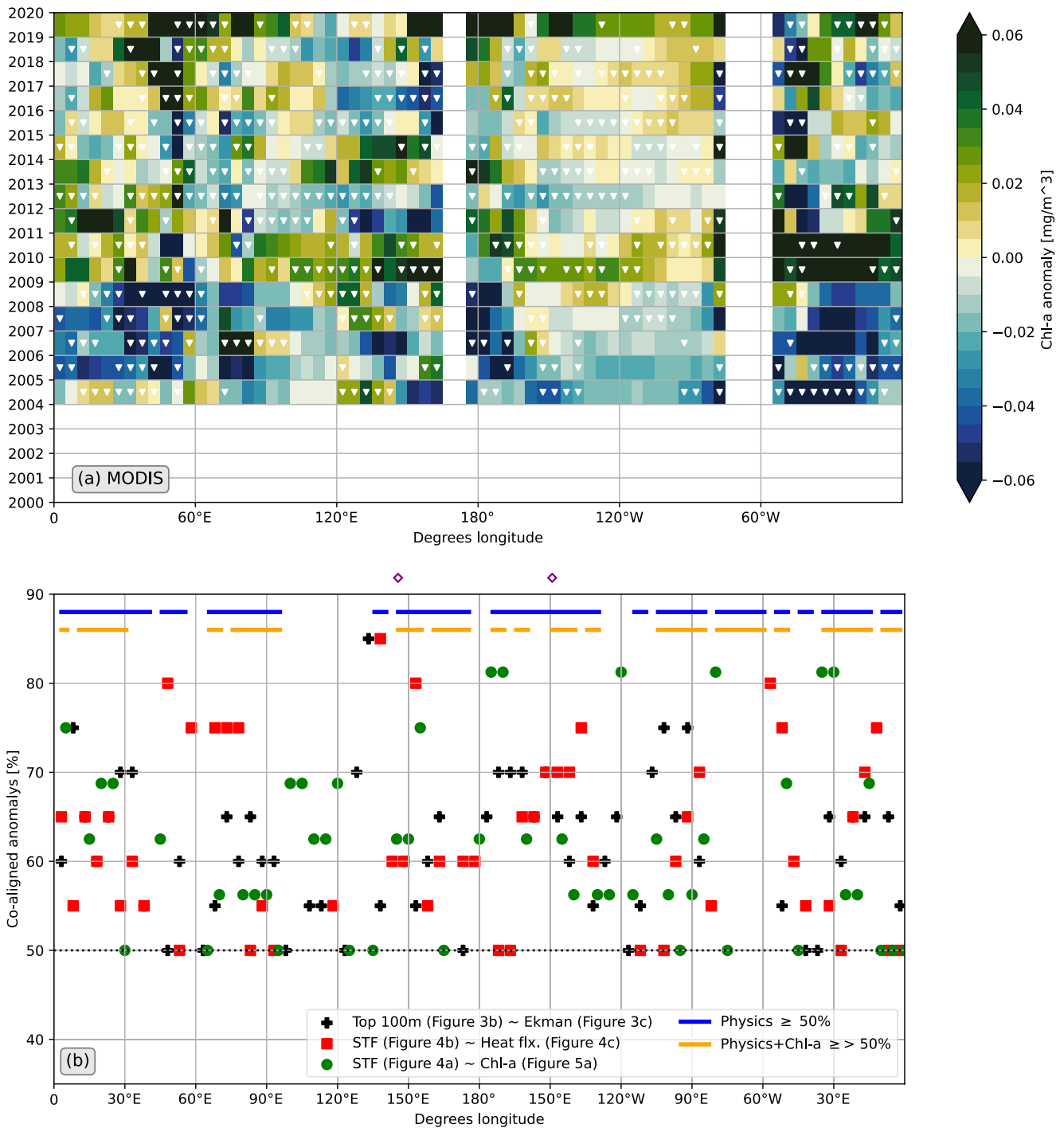


**Figure 5.** (a) MODIS chlorophyll-a anomaly relative to the period 2004–2019. White triangles in (a) indicate where the sign of Chl-a and Argo STF (Figure 4a) anomalies does not align with the concept in Figure 1. (b) How often anomalies align (in %) between Ekman transport versus averaged top 100 m temperature in NZ20 (black +, see Figure 3), heat flux anomalies versus STF anomalies from NZ20 (red squares, see Figure 4) and Argo STF anomalies versus Chl-a anomalies (green dots, see Figures 4a and 5a) with the concept from Figure 1. Blue (orange) horizontal bar indicates where the black and red (and green) markers show at least an agreement of  $\geq 50\%$  over time at this longitude. Chl-a anomalies are extracted between the time mean Argo STF location (2004–2019) and  $5^\circ$  south of it. Observations and model results have been binned to  $5^\circ$  longitude bins. The two purple diamonds in (b) indicate the eastern and western boundary of nested region in NZ20, where model resolution has been refined around New Zealand.

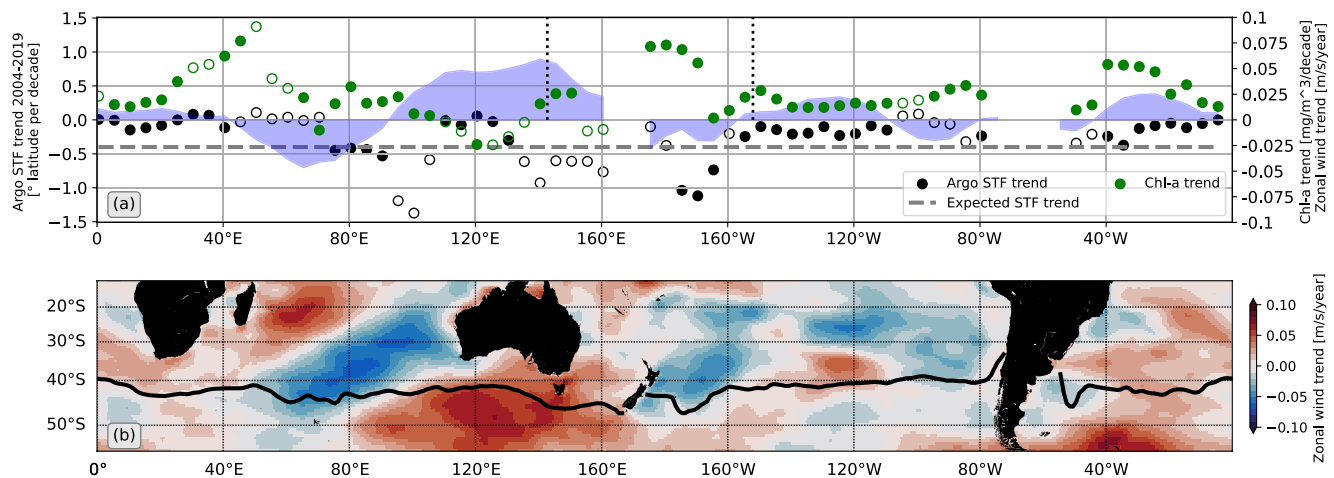


**Figure 6.** (a) Trends in the meridional location of the STF based on Argo temperature data from 2004 to 2019 (black circles), trends in Chl-a concentrations (green circles) and trends in the zonal winds (blue shading). Zonal wind trends are extracted over the mean location of the STF ( $\pm 2.5^\circ$  latitude band, 2004–2019), while the Chl-a trends are the average Chl-a anomaly over a  $5^\circ$  latitude band south of the mean STF location. Filled black circles indicate where the sign of zonal wind trends can explain the deviation of the actual STF trend from the expected trend ( $-0.4^\circ$  per decade, gray dashed line). Open black circles indicate the opposite. Filled green circles indicate where the sign of the actual STF trend aligns with the Chl-a trend with Figure 1, where a southward trend of the STF should result in positive Chl-a to the south of the STF. The blue shading is the zonal wind trend over the STF (see Figure 4b). (b) Zonal wind trend from JRA-55-DO from 2004 to 2019 is shown by the color shading and Argo mean STF location by the black line.

et al., 2019; Montie et al., 2020) suggest an increase in biological productivity in the Southern Ocean over the past decades, based on increasing Chl-a concentrations and a positive link to temperature. This increase has implications for the foodweb, and the fisheries of the STF. However, how these Chl-a trends will impact fish, fisheries, and the biological carbon pump is complex and not well understood. Nevertheless, future climate projections suggest that southernmost western boundary currents will further intensify (Qu et al., 2019; Sen Gupta et al., 2021), subtropical gyres will continue to expand poleward (Li et al., 2022; Yang et al., 2020) and marine heatwaves will become more intense and frequent and impact the STF (Behrens et al., 2022; Li et al., 2022; Oliver et al., 2019). More research is needed to robustly quantify the impacts of these physical changes on the biology and the ecosystems associated with the STF.

#### 4. Conclusions and Discussion

This paper explores how changes in surface winds can alter the location of the STF. We have tested how a southerly shift, or an increase of the westerly winds over the Southern Ocean can impact the meridional location of the STF. We tested if and where Ekman dynamics can be applied to explain the meridional shift in the STF and in which regions other drivers control the response.

In two sensitivity simulations a trend pattern to surface winds was applied over a 20-year period to investigate the transient response to these wind anomalies. The results from the sensitivity simulations and analyses of the past observed STF variability over the last 20 years have demonstrated that STF shifts, away from strong ocean currents, can be explained in the first-instance by changes in the Ekman transports as a consequence of the zonal wind stress anomalies over the STF ( $\pm 2.5^\circ$  longitude). Stronger westerly winds increase the northward Ekman transport and cause the STF to shift northward. Southward shifted winds, which results in locally reduced westerly winds reduces the Ekman transport and the STF shifts southward. However, the actual magnitude of the meridional displacement depends strongly on the local conditions (e.g., oceanic currents, stratification, and meridional temperature gradient). Nevertheless, regions where Ekman transport anomalies are largest tend to show the larger meridional displacements, than regions with weaker Ekman anomalies. However, the STF does not follow the Ekman response in regions where it interacts with ocean boundary currents. In these boundary current regions the STF is dominated by the Sverdrup balance, due to changes in the basin scale wind stress curl which offsets the positive Ekman anomalies. The intensification of the boundary current transports as a consequence of the Sverdrup changes leads to a southward shift of the STF while positive Ekman transport anomalies should result in the opposite northward shift. Other exceptions are regions where mesoscale eddy activity is high such as in the Agulhas Return Current. In these regions the STF does not show robust links with Ekman transport anomalies.

While the responses in the sensitivity simulations align with the expected response following Ekman theory the actual magnitude of anomalies might be compromised by using ocean-only simulations, with prescribed atmospheric boundary conditions. Using air temperatures and bulk formula to generate heat fluxes leads to a tight coupling between surface ocean and surface atmosphere temperatures (Griffies et al., 2009). It also limits the response to wind changes in the sensitivity simulations since the atmospheric temperatures remained unchanged in these sensitivity simulations compared to CONTROL. Consequently, the sensitivity simulations neglect atmospheric feedbacks, which dominate long-term (>decadal) response while the ocean memory controls the short-term response (Hewitt et al., 2017). A recent study has also demonstrated that changes in the buoyancy forcing can also impact the location of the boundary between subtropical and subantarctic gyre (Caneill et al., 2022). Coupled models are one way to include these feedbacks, but come with challenges of conducting these kind of sensitivity simulations without introducing artificial feedbacks.

Previous work has shown that model resolution has an impact on how realistic the STF can be modeled (Behrens et al., 2021). While the NZ20 nested configuration improved the STF representation in the southwest Pacific, it is likely that increased model resolution will improve the representation of the STF in other circumpolar regions.

Over the period 2004–2019 the observed southward trend of the STF is less than the expected southward trend in most regions, based on the overall southward shift of the zero wind stress curl and maximum in zonal winds, which both show a southward trend of 0.4° latitude per decade. We argue that the discrepancy between expected and actual shift of the STF could be explained by trends in the zonal winds, which are asymmetric and oppose the southward trend caused by the shift in some regions. The regions where local Ekman transports cannot explain the actual shift of the STF are very consistent between interannual and decade timescales and align with regions of mesoscale variability and strong oceanic currents such as in the vicinity of western boundary currents.

Changes in the location of the STF have profound implications on Chl-a concentrations, which provides motivation to improve our understanding about the physical driver of these STF shifts. A southward shifted STF generates negative Chl-a anomalies north of its previous STF position and positive Chl-a anomalies to its north, with implications on the local ecosystem and biological pump. A southward shift of the STF and the corresponding warmer water is the cause for the dipole response. A further warming of the Subtropical Water increases the stratification and reduces the nutrient supply, which goes along with decline in Chl-a. In Subantarctic Waters the deep mixed layers and/or strong vertical mixing causes light to be the limiting factor for phytoplankton growth (Boyd, 2002; Bradford-Grieve et al., 1999). Consequently, an increase in stratification and shallower mixed layers, due to warming in these waters leads to increases in Chl-a concentrations. While the sign of the Chl-a anomalies follows the direction of the STF shift, the magnitude of the Chl-a anomalies does not necessarily correspond to the magnitude of the STF shift. Here, the local conditions (e.g., nutrient concentrations) are important. Nevertheless, the impact on boundary current transports and Chl-a might be more nuanced due to the asymmetry of wind trends over the Southern Ocean (Beal & Elipot, 2016; Goyal et al., 2021; Noh et al., 2021; Sallée et al., 2010; Waugh et al., 2020), which results in regional variations. Here more regional and atmospheric coupled studies are needed to understand the local response.

#### Acknowledgments

This paper obtained funding and support through the Royal Society Marsden Fund (NIW1701) and funding from the Ministry of Business, Innovation and Employment through the Deep South National Science Challenge (C01X1902). We like to acknowledge the input from Andy Hogg (Australian National University) and Matthew England (University of New South Wales). We acknowledge the effort and time of the two anonymous reviewers to improve our manuscript. We would like to acknowledge the collaboration with MetOffice (UK) and the NeSI High Performance Computing Facility team for their technical support. Finally, I would like to acknowledge my partner, son, and daughter. Data used for this study can be freely accessed through: <https://doi.org/10.5281/zenodo.6837010>. Open access publishing facilitated by National Institute of Water and Atmospheric Research, as part of the Wiley - National Institute of Water and Atmospheric Research agreement via the Council of Australian University Librarians.

#### Data Availability Statement

Data used for this study can be freely accessed through: <https://doi.org/10.5281/zenodo.6837010>.

#### References

- Barnier, B., Madec, G., Penduff, T., Molines, J. M., Treguier, A. M., Le Sommer, J., et al. (2006). Impact of partial steps and momentum advection schemes in a global ocean circulation model at eddy-permitting resolution. *Ocean Dynamics*, 56(5–6), 543–567. <https://doi.org/10.1007/s10236-006-0082-1>
- Beal, L. M., & Elipot, S. (2016). Broadening not strengthening of the Agulhas Current since the early 1990s. *Nature*, 540(7634), 570–573. <https://doi.org/10.1038/nature19853>
- Behrens, E., Hogg, A. M., England, M. H., & Bostock, H. (2021). Seasonal and interannual variability of the Subtropical Front in the New Zealand region. *Journal of Geophysical Research: Oceans*, 126(2), e2020JC016412. <https://doi.org/10.1029/2020jc016412>
- Behrens, E., Rickard, G., Morgenstern, O., Martin, T., Osprey, A., & Joshi, M. (2016). Southern Ocean deep convection in global climate models: A driver for variability of subpolar gyres and Drake Passage transport on decadal timescales. *Journal of Geophysical Research: Oceans*, 121(6), 3905–3925. <https://doi.org/10.1002/2015jc011286>
- Behrens, E., Rickard, G., Rosier, S., Williams, J., Morgenstern, O., & Stone, D. (2022). Projections of future marine heatwaves for the oceans around New Zealand using New Zealand's Earth system model. *Frontiers in Climate*, 4. <https://doi.org/10.3389/fclim.2022.798287>
- Belkin, I. M. (2021). Subtropical frontal zone of the Southern Ocean.

- Belkin, I. M., & Gordon, A. L. (1996). Southern Ocean fronts from the Greenwich meridian to Tasmania. *Journal of Geophysical Research*, *101*(C2), 3675–3696. <https://doi.org/10.1029/95jc02750>
- Boyd, P. W. (2002). Environmental factors controlling phytoplankton processes in the Southern Ocean. *Journal of Phycology*, *38*(5), 844–861. <https://doi.org/10.1046/j.1529-8817.2002.t01-1-01203.x>
- Bradford-Grieve, J. M., Boyd, P. W., Chang, F. H., Chiswell, S., Hadfield, M., Hall, J. A., et al. (1999). Pelagic ecosystem structure and functioning in the Subtropical Front region east of New Zealand in austral winter and spring 1993. *Journal of Plankton Research*, *21*(3), 405–428. <https://doi.org/10.1093/plankt/21.3.405>
- Caneill, R., Roquet, F., Madec, G., & Nycander, J. (2022). The polar transition from alpha to beta regions set by a surface buoyancy flux inversion. *Journal of Physical Oceanography*, *52*(8), 1887–1902. <https://doi.org/10.1175/jpo-d-21-0295.1>
- Carranza, M. M., & Gille, S. T. (2015). Southern Ocean wind-driven entrainment enhances satellite chlorophyll-a through the summer. *Journal of Geophysical Research: Oceans*, *120*(1), 304–323. <https://doi.org/10.1002/2014jc010203>
- Chapman, C. C., Lea, M.-A., Meyer, A., Sallée, J.-B., & Hindell, M. (2020). Defining Southern Ocean fronts and their influence on biological and physical processes in a changing climate. *Nature Climate Change*, *10*(3), 209–219. <https://doi.org/10.1038/s41558-020-0705-4>
- Chiswell, S. M., Bradford-Grieve, J., Hadfield, M. G., & Kennan, S. C. (2013). Climatology of surface chlorophyll a, autumn-winter and spring blooms in the southwest Pacific Ocean. *Journal of Geophysical Research: Oceans*, *118*(2), 1003–1018. <https://doi.org/10.1002/jgrc.20088>
- Deacon, G. E. R. (1982). Physical and biological zonation in the Southern Ocean. *Deep-Sea Research*, *29*, 1–15. [https://doi.org/10.1016/0198-0149\(82\)90058-9](https://doi.org/10.1016/0198-0149(82)90058-9)
- De Boer, A. M., Graham, R. M., Thomas, M. D., & Kohfeld, K. E. (2013). The control of the Southern Hemisphere Westerlies on the position of the Subtropical Front. *Journal of Geophysical Research: Oceans*, *118*(10), 5669–5675. <https://doi.org/10.1002/jgrc.20407>
- Debreu, L., Vouland, C., & Blayo, E. (2008). AGRIF: Adaptive grid refinement in Fortran. *Computers & Geosciences*, *34*(1), 8–13. <https://doi.org/10.1016/j.cageo.2007.01.009>
- Del Castillo, C. E., Signorini, S. R., Karaköylü, E. M., & Rivero-Calle, S. (2019). Is the Southern Ocean getting greener? *Geophysical Research Letters*, *46*(11), 6034–6040. <https://doi.org/10.1029/2019gl083163>
- Frankcombe, L. M., Spence, P., Hogg, A. M., England, M. H., & Griffies, S. M. (2013). Sea level changes forced by Southern Ocean winds. *Geophysical Research Letters*, *40*(21), 5710–5715. <https://doi.org/10.1002/2013gl058104>
- Gaspar, P., Grégoris, Y., & Lefevre, J. M. (1990). A simple eddy kinetic energy model for simulations of the oceanic vertical mixing: Tests at station Papa and long-term upper ocean study site. *Journal of Geophysical Research*, *95*(C9), 16179–16193. <https://doi.org/10.1029/jc095ic09p16179>
- Good, S. A., Martin, M. J., & Rayner, N. A. (2013). EN4: Quality controlled ocean temperature and salinity profiles and monthly objective analyses with uncertainty estimates. *Journal of Geophysical Research: Oceans*, *118*(12), 6704–6716. <https://doi.org/10.1002/2013jc009067>
- Goyal, R., England, M. H., Jucker, M., & Sen Gupta, A. (2021). Response of Southern Hemisphere western boundary current regions to future zonally symmetric and asymmetric atmospheric changes. *Journal of Geophysical Research: Oceans*, *126*(11), e2021JC017858. <https://doi.org/10.1029/2021jc017858>
- Graham, R. M., de Boer, A. M., Heywood, K. J., Chapman, M. R., & Stevens, D. P. (2012). Southern Ocean fronts: Controlled by wind or topography? *Journal of Geophysical Research*, *117*(C8), C08018. <https://doi.org/10.1029/2012jc007887>
- Griffies, S. M., Biastoch, A., Böning, C., Bryan, F., Danabasoglu, G., Chassignet, E. P., et al. (2009). Coordinated ocean-ice reference experiments (COREs). *Ocean Modelling*, *26*(1–2), 1–46. <https://doi.org/10.1016/j.ocemod.2008.08.007>
- Hewitt, H. T., Bell, M. J., Chassignet, E. P., Czaja, A., Ferreira, D., Griffies, S. M., et al. (2017). Will high-resolution global ocean models benefit coupled predictions on short-range to climate timescales? *Ocean Modelling*, *120*, 120–136. <https://doi.org/10.1016/j.ocemod.2017.11.002>
- Hunke, E. C., & Lipscomb, W. H. (2010). CICE: The Los Alamos sea ice model, documentation and software user's manual, version 4.1. Knauss, J. A., & Garfield, N. (2016). *Introduction to physical oceanography*. Waveland Press.
- Law, C. S., Rickard, G. J., Mikaloff-Fletcher, S. E., Pinkerton, M. H., Behrens, E., Chiswell, S. M., & Currie, K. (2017). Climate change projections for the surface ocean around New Zealand. *New Zealand Journal of Marine and Freshwater Research*, 1–27.
- Lenn, Y.-D., & Chereskin, T. K. (2009). Observations of Ekman currents in the Southern Ocean. *Journal of Physical Oceanography*, *39*(3), 768–779. <https://doi.org/10.1175/2008jpo3943.1>
- Li, J., Roughton, M., & Kerry, C. (2022). Drivers of ocean warming in the western boundary currents of the Southern Hemisphere. *Nature Climate Change*, *12*(10), 901–909. <https://doi.org/10.1038/s41558-022-01473-8>
- Lovenduski, N. S., & Gruber, N. (2005). Impact of the southern annular mode on Southern Ocean circulation and biology. *Geophysical Research Letters*, *32*(11), L11603. <https://doi.org/10.1029/2005gl022727>
- Madec, G., Bourdallé-Badie, R., Bouttier, P.-A., Bricaud, C., Bruciaferri, D., Calvert, D., et al. (2017). NEMO ocean engine.
- Montie, S., Thomsen, M. S., Rack, W., & Broady, P. A. (2020). Extreme summer marine heatwaves increase chlorophyll a in the Southern Ocean. *Antarctic Science*, *32*(6), 508–509. <https://doi.org/10.1017/s0954102020000401>
- Noh, K. M., Lim, H.-G., & Kug, J.-S. (2021). Zonally asymmetric phytoplankton response to the Southern annular mode in the marginal sea of the Southern Ocean. *Scientific Reports*, *11*(1), 10266. <https://doi.org/10.1038/s41598-021-89720-4>
- Oliver, E. C. J., Burrows, M. T., Donat, M. G., Sen Gupta, A., Alexander, L. V., Perkins-Kirkpatrick, S. E., et al. (2019). Projected marine Heatwaves in the 21st century and the potential for ecological impact. *Frontiers in Marine Science*, *6*, 734. <https://doi.org/10.3389/fmars.2019.00734>
- Orsi, A. H., Whitworth, T., & Nowlin, W. D. (1995). On the meridional extent and fronts of the Antarctic Circumpolar Current. *Deep Sea Research Part I*, *42*(5), 641–673. [https://doi.org/10.1016/0967-0637\(95\)00021-w](https://doi.org/10.1016/0967-0637(95)00021-w)
- Pinkerton, M., Richardson, K., Boyd, P., Gall, M., Zeldis, J., Oliver, M., & Murphy, R. (2005). Intercomparison of ocean colour band-ratio algorithms for chlorophyll concentration in the Subtropical Front east of New Zealand. *Remote Sensing of Environment*, *97*(3), 382–402. <https://doi.org/10.1016/j.rse.2005.05.004>
- Qu, T. D., Fukumori, I., & Fine, R. A. (2019). Spin-up of the Southern Hemisphere Super Gyre. *Journal of Geophysical Research: Oceans*, *124*(1), 154–170. <https://doi.org/10.1029/2018jc014391>
- Rintoul, S. R., & England, M. H. (2002). Ekman transport dominates local air–sea fluxes in driving variability of Subantarctic Mode Water. *Journal of Physical Oceanography*, *32*(5), 1308–1321. [https://doi.org/10.1175/1520-0485\(2002\)032<1308:etdla>2.0.co;2](https://doi.org/10.1175/1520-0485(2002)032<1308:etdla>2.0.co;2)
- Roemmich, D., & Gilson, J. (2009). The 2004–2008 mean and annual cycle of temperature, salinity, and steric height in the global ocean from the Argo Program. *Progress in Oceanography*, *82*(2), 81–100. <https://doi.org/10.1016/j.pocan.2009.03.004>
- Sallée, J. B., Speer, K. G., & Rintoul, S. R. (2010). Zonally asymmetric response of the Southern Ocean mixed-layer depth to the southern annular mode. *Nature Geoscience*, *3*(4), 273–279. <https://doi.org/10.1038/ngeo812>
- Sathyendranath, S., Brewin, R. J., Brockmann, C., Brotas, V., Calton, B., Chuprin, A., et al. (2019). An ocean-colour time series for use in climate studies: The experience of the ocean-colour climate change initiative (OC-CCI). *Sensors*, *19*, 4285. <https://doi.org/10.3390/s19194285>

- Sen Gupta, A., Stellema, A., Pontes, G. M., Taschetto, A. S., Vergés, A., & Rossi, V. (2021). Future changes to the upper ocean Western Boundary Currents across two generations of climate models. *Scientific Reports*, *11*(1), 9538. <https://doi.org/10.1038/s41598-021-88934-w>
- Shears, N. T., & Bowen, M. M. (2017). Half a century of coastal temperature records reveal complex warming trends in western boundary currents. *Scientific Reports*, *7*(1), 14527. <https://doi.org/10.1038/s41598-017-14944-2>
- Smale, D. A., Wernberg, T., Oliver, E. C., Thomsen, M., Harvey, B. P., Straub, S. C., et al. (2019). Marine heatwaves threaten global biodiversity and the provision of ecosystem services. *Nature Climate Change*, *9*(4), 306–312. <https://doi.org/10.1038/s41558-019-0412-1>
- Sokolov, S., & Rintoul, S. R. (2009). Circumpolar structure and distribution of the Antarctic Circumpolar Current fronts: 1. Mean circumpolar paths. *Journal of Geophysical Research*, *114*(C11), C11018. <https://doi.org/10.1029/2008jc005108>
- Spence, P., Fyfe, J. C., Montenegro, A., & Weaver, A. J. (2010). Southern Ocean response to strengthening winds in an eddy-permitting global climate model. *Journal of Climate*, *23*(19), 5332–5343. <https://doi.org/10.1175/2010jcli3098.1>
- Spence, P., Griffies, S. M., England, M. H., Hogg, A. M., Saenko, O. A., & Jourdain, N. C. (2014). Rapid subsurface warming and circulation changes of Antarctic coastal waters by poleward shifting winds. *Geophysical Research Letters*, *41*(13), 4601–4610. <https://doi.org/10.1002/2014gl060613>
- Storkey, D., Blaker, A. T., Mathiot, P., Megann, A., Aksenov, Y., Blockley, E. W., et al. (2018). UK Global Ocean GO6 and GO7: A traceable hierarchy of model resolutions. *Geoscientific Model Development*, *11*(8), 3187–3213. <https://doi.org/10.5194/gmd-11-3187-2018>
- Sullivan, C. W., Arrigo, K. R., McClain, C. R., Comiso, J. C., & Firestone, J. (1993). Distributions of phytoplankton blooms in the Southern Ocean. *Science*, *262*(5141), 1832–1837. <https://doi.org/10.1126/science.262.5141.1832>
- Swart, N. C., & Fyfe, J. C. (2012). Observed and simulated changes in the Southern Hemisphere surface westerly wind-stress. *Geophysical Research Letters*, *39*(16), L16711. <https://doi.org/10.1029/2012gl052810>
- Thompson, A. F., & Sallée, J.-B. (2012). Jets and topography: Jet transitions and the impact on transport in the Antarctic Circumpolar Current. *Journal of Physical Oceanography*, *42*(6), 956–972. <https://doi.org/10.1175/jpo-d-11-0135.1>
- Tilburg, C. E., Hurlburt, H. E., O'Brien, J. J., & Shriver, J. F. (2002). Remote topographic forcing of a baroclinic western boundary current: An explanation for the Southland Current and the pathway of the Subtropical Front east of New Zealand. *Journal of Physical Oceanography*, *32*(11), 3216–3232. [https://doi.org/10.1175/1520-0485\(2002\)032<3216:rtfoab>2.0.co;2](https://doi.org/10.1175/1520-0485(2002)032<3216:rtfoab>2.0.co;2)
- Tsujino, H., Urakawa, S., Nakano, H., Small, R. J., Kim, W. M., Yeager, S. G., et al. (2018). JRA-55 based surface dataset for driving ocean–sea-ice models (JRA55-do). *Ocean Modelling*, *130*, 79–139. <https://doi.org/10.1016/j.ocemod.2018.07.002>
- Wang, W., & Huang, R. X. (2004). Wind energy input to the Ekman layer. *Journal of Physical Oceanography*, *34*(5), 1267–1275. [https://doi.org/10.1175/1520-0485\(2004\)034<1267:weitte>2.0.co;2](https://doi.org/10.1175/1520-0485(2004)034<1267:weitte>2.0.co;2)
- Waugh, D. W., Banerjee, A., Fyfe, J. C., & Polvani, L. M. (2020). Contrasting recent trends in Southern Hemisphere westerlies across different ocean basins. *Geophysical Research Letters*, *47*(18), e2020GL088890. <https://doi.org/10.1029/2020gl088890>
- Weeks, S. J., & Shillington, F. A. (1994). Interannual scales of variation of pigment concentrations from coastal zone color scanner data in the Benguela Upwelling system and the Subtropical Convergence zone south of Africa. *Journal of Geophysical Research*, *99*(C4), 7385–7399. <https://doi.org/10.1029/93jc02143>
- Wu, L., Cai, W., Zhang, L., Nakamura, H., Timmermann, A., Joyce, T., et al. (2012). Enhanced warming over the global subtropical western boundary currents. *Nature Climate Change*, *2*(3), 161–166. <https://doi.org/10.1038/nclimate1353>
- Yang, H., Lohmann, G., Krebs-Kanzow, U., Ionita, M., Shi, X., Sidorenko, D., et al. (2020). Poleward shift of the major ocean gyres detected in a warming climate. *Geophysical Research Letters*, *47*(5), e2019GL085868. <https://doi.org/10.1029/2019gl085868>

## References From the Supporting Information

- Beal, L. M., & Bryden, H. L. (1999). The velocity and vorticity structure of the Agulhas Current at 32°S. *Journal of Geophysical Research*, *104*(C3), 5151–5176. <https://doi.org/10.1029/1998JC900056>
- Behrens, E., Fernandez, D., & Sutton, P. (2019). Meridional oceanic heat transport influences marine heatwaves in the Tasman Sea on interannual to decadal timescales. *Frontiers in Marine Science*, *6*, 228. <https://doi.org/10.3389/fmars.2019.00228/abstract>
- Hill, K. L., Rintoul, S. R., Coleman, R., & Ridgway, K. R. (2008). Wind forced low frequency variability of the East Australia Current. *Geophysical Research Letters*, *35*(8), L08602. <https://doi.org/10.1029/2007GL032912>
- Mata, M. M., Tomczak, M., Wijffels, S., & Church, J. A. (2000). East Australian Current volume transports at 30°S: Estimates from the World Ocean Circulation Experiment hydrographic sections PR11/P6 and the PCM3 current meter array. *Journal of Geophysical Research*, *105*(C12), 28509–28526. <https://doi.org/10.1029/1999JC000121>
- Oliver, E. C. J., & Holbrook, N. J. (2014). Extending our understanding of South Pacific gyre “spin-up”: Modeling the East Australian Current in a future climate. *Journal of Geophysical Research: Oceans*, *119*(5), 2788–2805. <https://doi.org/10.1002/2013JC009591>
- Spadone, A., & Provost, C. (2009). Variations in the Malvinas Current volume transport since October 1992. *Journal of Geophysical Research*, *114*(C2), C02002. <https://doi.org/10.1029/2008JC004882>
- Stanton, B., & Sutton, P. (2003). Velocity measurements in the East Auckland Current north-east of North Cape, New Zealand. *New Zealand Journal of Marine & Freshwater Research*, *37*(1), 195–204. <https://doi.org/10.1080/00288330.2003.9517157>